Proceedings of ASME Turbo Expo 2011
GT2011
June 6-10, 2011, Vancouver, British Columbia, Canada

GT2011-46214

COMPUTATIONAL FLUID DYNAMICS DRAG PREDICTION AND DECOMPOSITION FOR PROPULSIVE SYSTEM INTEGRATION

Thierry Sibilli
Cranfield University
Department Power & Propulsion
MK43 0AL Cranfield, Bedfordshire,
United Kingdom
Email: t.sibilli@cranfield.ac.uk

Mark Savill
Cranfield University
Department Power & Propulsion
MK43 0AL Cranfield, Bedfordshire,
United Kingdom
Email: mark.savill@cranfield.ac.uk

ABSTRACT

The prediction and decomposition of drag associated to Propulsive System Integration (PSI) is investigated applying a methodology based on entropy variations in the flow and the momentum conservation theorem. This advanced prediction method can decompose the total drag in to viscous, wave, induced and spurious drag, allowing a better understanding of the flow. The spurious drag, due to numerical errors, can be eliminated reducing the dependency of the solution on the grid quality. Four applications are presented: two wing-body configurations, a wing-body-nacelle-pylon with trough-flow-nacelle, and a wing-body-nacelle-pylon with a very-high-bypass-ratio engine in power-on condition. One objective is to minimize grid resolution to enable design optimization.

INTRODUCTION

The present economic situation increases the pressure on commercial aviation companies to reduce the Direct Operating Cost, and the environmental situation require a new generation of aircraft with a lower environmental impact. Therefore, engine and aircraft manufactures, research centres and universities are making great efforts to reduce the drag of the complete aircraft and thereby to achieve a lower fuel consumption.

On the engine side, the achievement of these objectives requires an increase of the total efficiency of the current power plants and one solution is to increase the Bypass Ratio (BR). Early wing mounted installations of High Bypass Ratio (HBR) engines allowed enough distance from the wing to avoid excessive drag penalties, but now with the increase in size from HB to Very High (VHBR) or Ultra High Bypass Ratio (UHBR), it is necessary to position engines closer to the wing in order to both maintain the current ground clearance and to avoid extending the already heavy main landing gear legs. The potential fuel reduction of these engines must therefore take in to count the installation penalties, this leads to the need to study and understand the effects of wing-mounted engine installations[1-2], evaluating the drag related to the different configurations. However the prediction of drag in CFD is still a big challenge and in spite of the rapid development of numerical schemes and computing power the challenge is still open[3]. One of the major issues responsible for this remains computational mesh dependency; reliable results need fine meshes.

The quality of the grid is directly related to the numerical dissipation and discretization errors that generate spurious drag, increasing the difference between the numerical solution and the real flow.

To overcome this problem different approaches were proposed[4-6], and in particular one of them has recently gained interest: the *mid-field method*.

This method is intended to offer a substitute to the traditional *near-field method* that computes the drag by performing a surface integration of pressure and stress tensor, integrating entropy drag and related quantity on defined volumes and planes around the body[7]. The approach is based on the *far-field method* in which the drag is calculated by applying a momentum balance evaluated on a surface far from the body[4]. The application of Gauss's theorem, to obtain a volume integral formulation, allows one to limit the integration in parts of the control volume where the entropy drag has physical sources: boundary layers and shocks, and therefore to identify and eliminate the spurious drag.

This method substantially reduces the numerical error associated with poor quality meshes compared to the *near-field method*. Another intrinsic advantage of this technique is the drag breakdown capability which allows a better understanding of the flow around the body.

The paper gives a brief introduction to this methodology showing its suitability for PSI, and ends with four numerical applications: two wing-body configurations (WB), a wing-body-nacelle-pylon with trough-flow-nacelle (WBNP-TF), and a wing-body-nacelle-pylon with a VHBPR engine in power-on condition (WBNP-PO). The object of this work is to asses the capability of the *mid-field method* for PSI, that potentially increases the accuracy of the drag evaluation and simplify the way to do it at the same time[8-9].

DRAG ESTIMATION

Applying the momentum balance for a steady flow with free stream velocity V_∞, on a volume that surrounds an unpowered aircraft, we can define the aerodynamic force as:

$$F = \int_{S_{body}} [(p - p_\infty) - (\boldsymbol{\tau}_w \cdot \boldsymbol{n})] dS$$
$$= -\int_{S_{far}} [\rho V \boldsymbol{V} + (p - p_\infty) V - \boldsymbol{\tau}_w] \cdot \boldsymbol{n}\, dS \qquad (1)$$

Showing that we can evaluate the force in two different ways: integration the pressure and stress tensor on the body surface of aircraft (left equation), or evaluation the net momentum flux across the surface S_{far} (right equation), located far from the body. The first integral is used by the well know *near-field method* and the second one to derive the *far-field method*.

Expanding the second integral in Taylor's series with respect to the pressure, entropy and total enthalpy, it is possible to obtain the so called entropy drag[7] (eqn. 2), the first term of the expansion that only for a two-dimensional adiabatic flow, represent the total drag. The second term, related to enthalpy variations, is negligible on power-off conditions.

$$D_{\Delta s} = -V_\infty \int_{S_{far}} \rho\, g(\Delta s/R)(\boldsymbol{V} \cdot \boldsymbol{n}) dS \qquad (2)$$

With:

$$g = cs1\left(\frac{\Delta s}{R}\right) \qquad (3)$$

Where Δs is the entropy variation respect to the free-stream condition and the *cs1* coefficient, coming from the Taylor's expansion, is:

$$c_{s1} = -\frac{V_\infty}{\gamma M_\infty^2} \qquad (4)$$

Applying the Gauss's divergence theorem to the vector field $\rho g \boldsymbol{V}$ in the finite flow domain **Ω**, equation (2) becomes:

$$D_{\Delta s} = V_\infty \int_\Omega \nabla \cdot (\rho g \boldsymbol{V})\, d\Omega \qquad (5)$$

It is convenient to express the vector $\rho g \boldsymbol{V}$ as:

$$\boldsymbol{f}_{vw} = -\rho g \boldsymbol{V} \qquad (6)$$

Decomposing the domain $\boldsymbol{\Omega}$ in shock waves volume $\boldsymbol{\Omega}_s$, viscous volume $\boldsymbol{\Omega}_v$, and spurious volume $\boldsymbol{\Omega}_{sp}$, the entropy drag can be defined as:

$$D_{\Delta s} = D_v + D_w + D_{sp} \qquad (7)$$

Where:

$$D_v = V_\infty \int_{\Omega_v} \nabla \cdot \boldsymbol{f}_{vw} d\Omega\,, \qquad D_w = V_\infty \int_{\Omega_w} \nabla \cdot \boldsymbol{f}_{vw} d\Omega$$

$$D_{sp} = V_\infty \int_{\Omega_{sp}} \nabla \cdot \boldsymbol{f}_{vw} d\Omega \qquad (8)$$

The drag can therefore be evaluated separately for each component.

The selection of the respective volumes is computed using selectors proposed by Tognaccini[7]. The shock wave zone is based on the non dimensional function:

$$F_{shock} = \frac{V \cdot \nabla p}{a|\nabla p|} > 0 \qquad (9)$$

Where *a* is the sound speed. We can notice that sensor will be negative in expansion zones and positive in compression zones. Hence cells with negative F_{shock} can be excluded from the wake region.

The boundary-layer and wake region is selected using a sensor based on the eddy viscosity:

$$F_{visc} = \frac{\mu_t}{\mu_l} + 1 \tag{10}$$

Where μ_l and μ_t are respectively the laminar and eddy viscosities. The value of F_{visc} will be very high in the viscous zone and ≈ 1 in the other zones. Hence the selection can be done applying:

$$F_{visc} > K_{visc} \cdot F_\infty \tag{11}$$

Where F_∞ is the value of eqn. (10) in the freestream condition, and K_{visc} is a cut-off parameter.

As pointed out the entropy drag, equal to the well-know Oswatitsch[10] expression, is different from the total drag for a three-dimensional adiabatic flow, due to the Taylor's first order approximation, being only related to the irreversible processes. To get the exact *near-field*/*mid-field* drag balance, the fourth drag component, the induced drag D_i, related to reversible processes, can be computed using the Van der Vooren's formulation[9]:

$$D_i = \int_{\Omega_v+\Omega_w} \nabla \cdot \boldsymbol{f_i} d\Omega - \int_{S_D} (\boldsymbol{f_i} \cdot \boldsymbol{n})\, dS \tag{12}$$

Where S_D is a downstream surface and $\boldsymbol{f_i}$ defined by:

$$\boldsymbol{f_i} = -\rho(u - u_\infty - g)\boldsymbol{V} - (p - p_\infty)\boldsymbol{n} + \tau_x \tag{13}$$

The total drag can now be computed as:

$$D = D_v + D_w + D_i + D_{sp} \tag{14}$$

Defining the vector $\boldsymbol{f}$ as:

$$\boldsymbol{f} = \boldsymbol{\rho V V} + (\boldsymbol{p} - \boldsymbol{p}_\infty)\boldsymbol{V} - \boldsymbol{\tau_w} \tag{15}$$

From equation (1) and (2)

$$\boldsymbol{f} = \boldsymbol{f}_{vw} + \boldsymbol{f}_i \tag{16}$$

Assuring the exact drag balance from the two different methods and given that $\nabla \cdot \boldsymbol{f} = 0$, equation (12) can be rewritten in a easier implementation formula:

$$D_i = -\int_{\Omega_v+\Omega_v} \nabla \cdot \boldsymbol{f_{vw}} d\Omega - \int_{S_{skin}} (\boldsymbol{f_i} \cdot \boldsymbol{n})\, dS \tag{17}$$

The assumptions may be violated in jet or propeller configurations therefore Van der Vooren proposed an alternative formulation for power-on configurations:

$$D_i = -\int_{\Omega_v+\Omega_w} \nabla \cdot \boldsymbol{f_{vw}} d\Omega - \int_{S_{aframe+engine}} (\boldsymbol{f_i} \cdot \boldsymbol{n})\, dS + \frac{1}{2}\int_{S_{engine}} \rho(v^2 + w^2) n_x dS \tag{18}$$

The correct drag-thrust bookkeeping is assured defining the engine, S_{engine} and airframe S_{aframe} domains[8,9,10].

The second set of calculations, showed at the end of this paper, is performed on a power-on condition, where the approximation of negligible enthalpy variations doesn't stand. However ref.8 and ref.9 pointed out that the entropy drag related to the external flow for power on condition (eqn.18) is the same as eqn.2, but with a different volume of integration. Note that the force associated to the total enthalpy variations is negligible outside the fan and core jets, therefore in the entropy drag can be written as:

$$D_{\Delta s} = V_\infty \int_{\Omega'} \nabla \cdot (\rho g \boldsymbol{V})\, d\Omega \tag{19}$$

Where $\boldsymbol{\Omega}'$ is the domain volume minus the inlet/jet flows volumes.

$$\Omega' = \Omega - \Omega_{pre} - \Omega_{jet} \tag{20}$$

Like the power-off condition the entropy drag can be decomposed in viscous, shock and spurious components. Once again to compute the total drag, the induced drag (eqn.18) is added to the other components.

TEST CASES

The selected geometries are: for the first set of results, the DLR-F6[12] WB and WBNP-TF, and for the second set the CRM[13] and WBNP-PO, with a VHBPR engine. The DLR-F6, (fig.1) used during the 2nd Drag Prediction Workshop[12], is a typical twin engine wide-body aircraft, with no fairing between the wing and the body, and for the WBNP-TF with low-bypass ratio engines. The design Mach number is 0.75, with a Reynolds number, based on the mean aerodynamic cord, of Re = 3×10^6. The CRM (Common Research Model fig.2) developed by the Boeing Company, and used during the 4th Drag Prediction Workshop[13], is a wing-body aircraft with a transonic supercritical wing and a fairing between the wing and the body.

The design Mach number is 0.85, with a Reynolds number, based on the mean aerodynamic cord, of Re = 5×10^6, a cruise lift coefficient of $C_L = 0.5$ and a bypass ratio of BPR=14. The pylon and nacelle, on the WBNP-PO configuration, are designed by the author to represent a typical VHBPR installation case.

For the DLR-F6 is possible to compare the numerical results with experimental data coming from test campaigns that have been performed in the ONERA S2MA pressurized wind tunnel in 1990[14].

NUMERICAL METHOD

The Reynolds Averaged Navier-Stokes (RANS) equations are discretized using a vertex-based finite volume method, and evaluated using a second-order advection scheme with a pressure-velocity coupling technique. The Reynolds stresses in the momentum equations, are computed using the Menter's Zonal two equations κ-ω turbulence model[15].

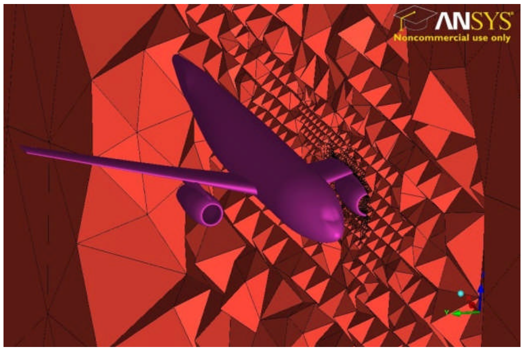

Fig. 1 DLR-F6 WBNP-TF configuration

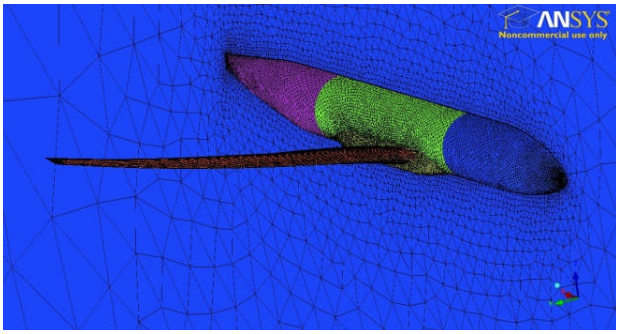

Fig. 2 CRM WB configuration

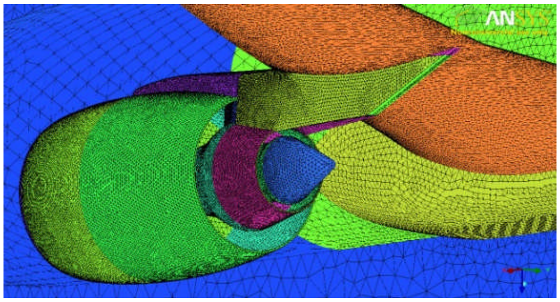

Fig. 3 PSI detail on CRM WBNP-PO configuration

The grids are hybrid type and have been constructed following the basic gridding guidelines proposed after the experience gained within drag prediction workshops[3]. Two grid levels are used for the DLR-F6: coarse grids with approximately 2×10^6 nodes for the WB and 3×10^6 nodes for the WBNP, and a medium grid with approximately 5×10^6 nodes for the WB and 5.5×10^6 nodes for the WBNP.

The results for the CRM case are computed using meshes of the order of 8×10^6 nodes for the WB, and 12×10^6 nodes for the WBNP-PO.

The selected meshes for the DLR-F6 cases are very coarse in order to allow a correct evaluation of the *mid-field* method potential. One objective of this study is to minimize grid resolution to enable automated PSI design optimization for future work. Figures 1,2, and 3 show the DLR's coarse WBNP grid and the CRM's WBNP-PO grid.

DLR-F6 RESULTS

The pressure coefficient computed with the coarse mesh, at various spanwise locations for the WB and WBNP, is plotted respectively in figures 4 and 5, showing good agreement between numerical and experimental results. The coarse and medium drag polar are presented in fig. 6 for the WB and fig. 7 for the WBNP-TF. The differences between numerical and experimental results are due to the low grid resolution, where a grid refinement is necessary to capture all the aerodynamic effects.

The WBNP-TF present higher discrepancy due to the more complicate geometry and therefore more complicated aerodynamics, analyzed by a intrinsically lower-quality mesh. Both configurations are potentially good applications to show the capability of the *mid-field* method.

The installation drag, show in fig.8, is computed from:

$$C_{D_{inst}} = C_{D_{WBNP-TF}} - C_{D_{WB}} - C_{D_{Int\,Nac}} \tag{21}$$

Where $C_{D_{Int\,Nac}}$ is the internal nacelle drag which was measured in calibrated tests[14].

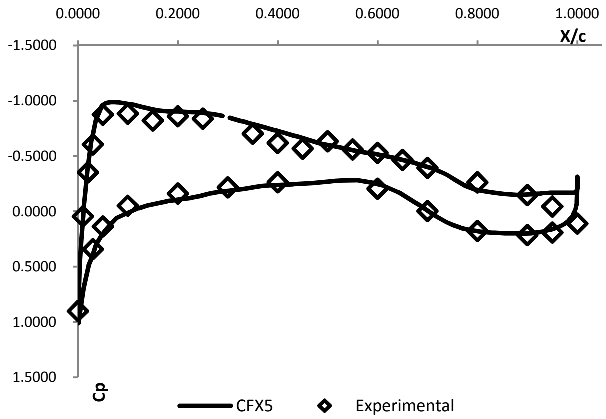

Fig. 4 Pressure @ Y/C = 0.15 for WB configuration

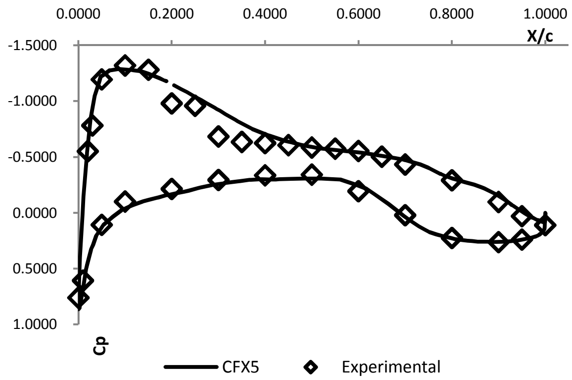

Fig. 5 Pressure @ Y/C = 0.239 for WBNP configuration

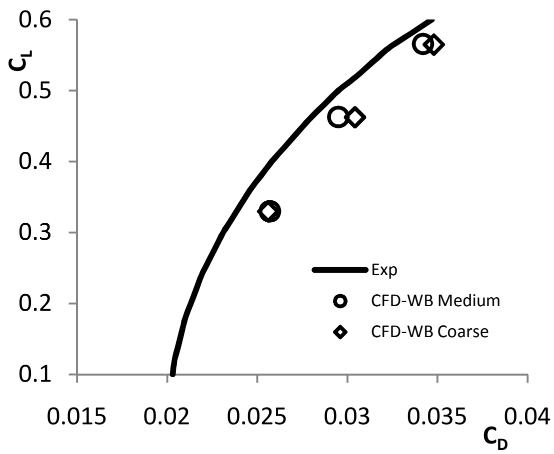

Fig. 6 Drag polar DLR-F6 WB configuration

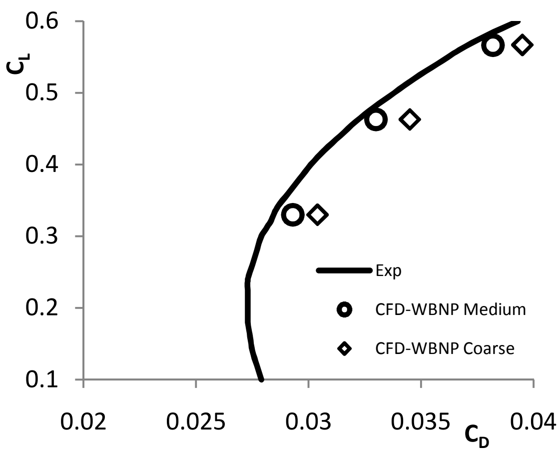

Fig. 7 Drag polar DLR-F6 WBNP-TF configuration

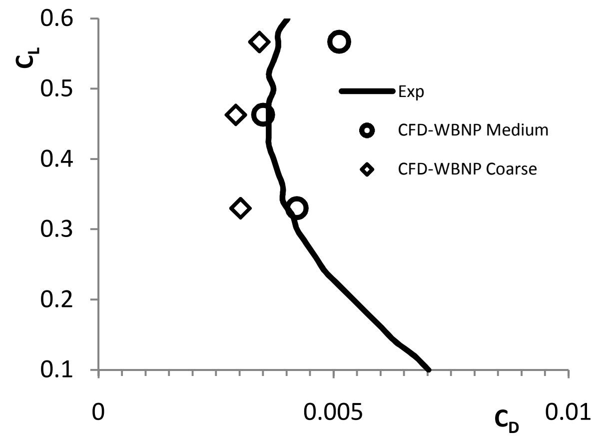

Fig. 8 Installation Drag polar DLR-F6 configuration

Using the selectors, (eq. 9-10), the viscous and shock volumes can be visualized as show in figures 9 and 10. Note the inboard pylon shock on fig. 10, revealing good agreement with the experimental results.

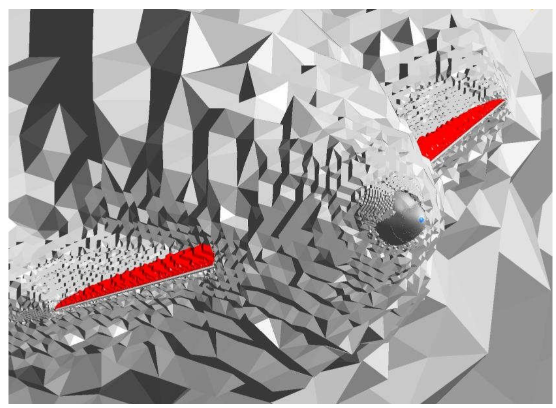

Fig. 9 Shock (red) and viscous (grey) volume selection for DLR-F6 WB configuration at C_L = 0.56

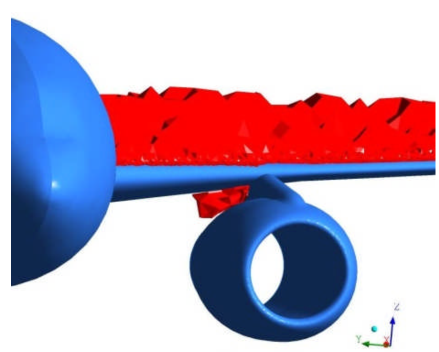

Fig. 10 Shock volume selection for DLR-F6 WBNP-TF configuration

In fig.11, 12, and 13 the *mid-field* drag decomposition results are shown, revealing that the methodology can predict viscous, shock and induced drag, isolating the spurious drag. The different components are plotted for the coarse and medium meshes, revealing that they are almost independent of the mesh size.

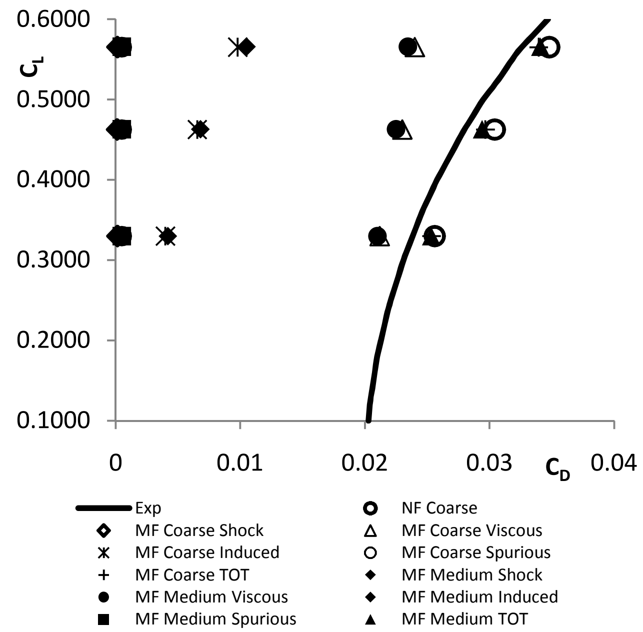

Fig. 11 Mid-field results for DLR-F6 WB configuration

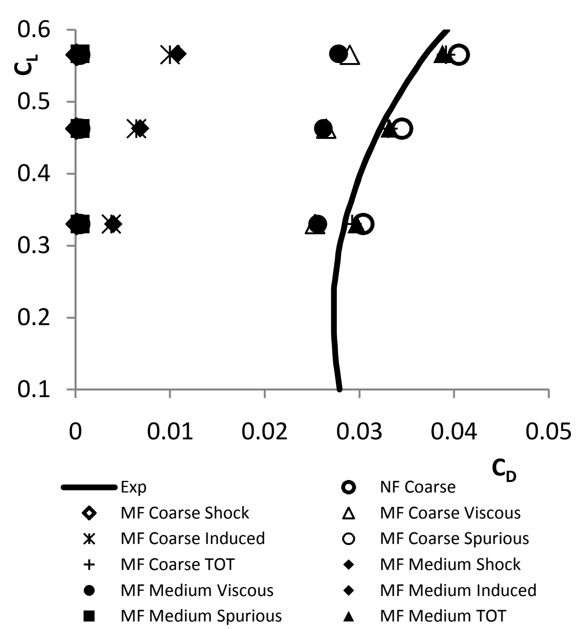

Fig. 12 Mid-field results for DLR-F6 WBNP configuration

This is confirmed in figure 14 and 15, showing lower uncertainty bands for the *mid-field* method respect to the *near-field* (h = 1 specify the finest grid size). From figure 11, 12 and 13 can be pointed out that the total *mid-field* drag estimation and the experimental results are in better agreement compared with the results extracted using the *near-field* method, in both WB and WBNP-TF configurations.

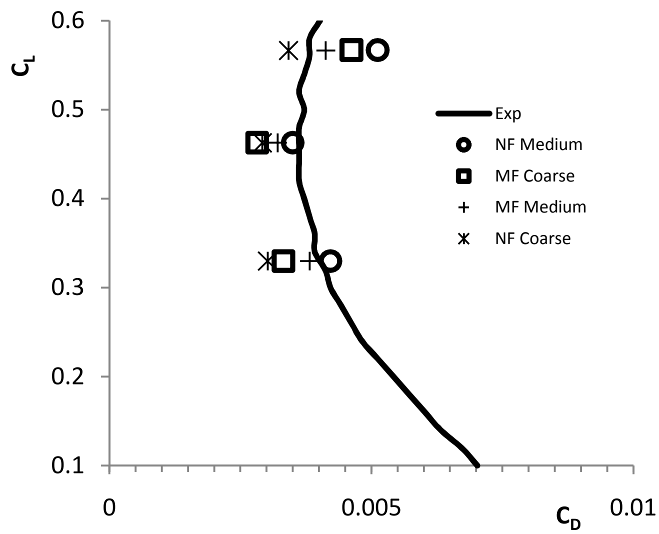

Fig. 13 *Mid-field* installation Drag polar DLR-F6 configuration

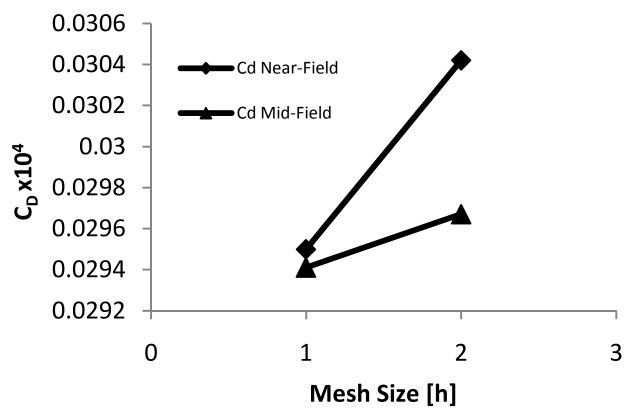

Fig. 14 Mid-field/Near-Field mesh size sensibility for DLR-F6 WB configuration

CRM RESULTS

The CRM PSI aerodynamics is characterized by a strong shock on the inboard side of the pylon, and a separation zone. This because the pylon and nacelle geometries still need to be refined in order to represent a standard PSI case.

The nacelle is asymmetric to reduce the complexity of the geometry and because of the lack of information at this state of the project. All of this assumption and simplification don't influence the assessment of the potential capability of the *mid-field* method on PSI applications.

To correctly evaluate the PSI installation drag and avoid double accounting, a proper thrust-and-drag bookkeeping is crucial, especially in a power-on configuration. In order to fulfill this requirement, the integration domain was divided as suggested by Tognaccini[8] and Van der Vooren[9].
The shock volume selection for the WBNP-PO configuration is showed in fig.16 confirming the presence of the strong shock on the inboard side.

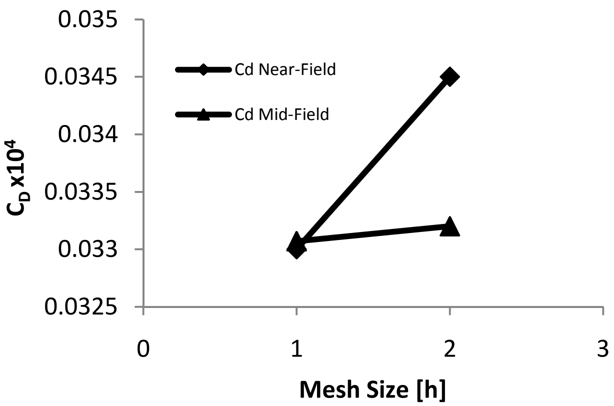

Fig. 15 Mid-field/Near-Field mesh size sensibility for DLR-F6 WBNP configuration

Table 1,2 and 3 summarize the results for the CRM WB and WBNP-PO configurations. The results look encouraging, allowing, again, to decompose and evaluate the spurious drag, increasing the reliability of the CFD results.
Form table 1 and 2 we can see that the spurious drag is higher on the WBNP-PO configuration due to the lower mesh quality associated to the more complicated geometry.

CL	**CD_{NF}**
0.485	0.0315

CL	CD_v	CD_w	CD_i	CD_{sp}	**CD_{TOTMF}**
0.485	0.0185	0.0011	0.0113	0.0006	0.0309

Table 1 *Mid-field/Near-Field* Drag CRM WB configuration

CL	**CD_{NF}**
0.495	0.0385

CL	CD_v	CD_w	CD_i	CD_{sp}	**CD_{TOTMF}**
0.495	0.0215	0.0025	0.0134	0.0009	0.0374

Table 2 *Mid-field/Near-Field* Drag CRM WBNP-PO configuration

CL	**CD_{NFinst}**	**CD_{MFinst}**
0.495	0.007	0.0065

Table 3 *Mid-field/Near-Field* Installation Drag CRM configuration

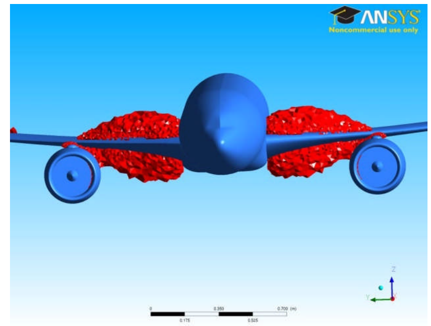

Fig. 16 Shock volume selection for CRM WBNP-PO configuration

CONCLUSIONS

The prediction and decomposition of drag associated to Propulsive System Integration (PSI) has been investigated applying a new methodology based on entropy variations in the flow and the momentum conservation theorem. The installation drag of two different aircrafts for a conventional and a VHBR nacelle in through flow and power on condition, respectively, has been evaluated showing better agreement with the experimental results than the classic *near-field* method. This because the spurious drag, due to numerical errors, can be eliminated reducing the dependency of the solution on the grid quality. The objective of this work was to minimize grid resolution to enable PSI design optimization, given that the computational effort on PSI application is very high, due to the complexity of the problem.

REFERENCES

[1] Oliveira, G.L., Puppin-Macedo,A. and Trapp, L.G., (2003), “Integration Methodology for Regional Jet Aircraft With Underwing Engines”. AIAA Paper 2003-0934.
[2] Rossow, C. -., Godard, J. -., Hoheisel, H. and Schmitt, V. (1992), "Investigations of Propulsion Integration Interference Effects on a Transport Aircraft Configuration", *AIAA, SAE, ASME, and ASEE, Joint Propulsion Conference and Exhibit*, 28th, Nashville, TN; UNITED STATES; 6-8 July 1992, AIAA-92-3097.
[3] Mavriplis, D. J., Vassberg, J. C., Tinoco, E. N., Mani, M., Brodersen, O. P., Eisfeld, B., Wahls, R. A., Morrison, J. H., Zickuhr, T., Levy, D. and Murayama, M. (2009), "Grid quality and resolution issues from the drag prediction workshop series", *Journal of Aircraft*, vol. 46, no. 3, pp. 935-950.
[4] Kusunose K. (1998) “Drag Prediction Based on Wake Integral Method”, AIAA Paper, Applied Aerodynamics Conference, 16th, Albuquerque, NM, June 15-18, 1998, AIAA-98-2723.
[5] Van Dam, C.P., “ Recent Experience with Different Methods of Drag Prediction”, *Progress in Aerospace* Sciences, vol.35, No.8, 1999, pp-751-798.

[6] Desterac, D, (2003) “Far-Field/Near-Field drag balance an applications of drag extraction in CFD”, *CFD-Based Aircraft Drag Prediction and Reduction*”, LS 2003-02, von Karman Inst. For Fluid Dynamics Lecture Series, von Karman Inst. for Fluid Dynamics, Rhode St-Genese, Belgium.
[7] Paparone, L. and Tognaccini, R. (2003), "Computational fluid dynamics-based drag prediction and decomposition", *AIAA Journal*, vol. 41, no. 9, pp. 1647-1657.
[8] Tognaccini, R. (2005), "Drag Computation and Breakdown in Power-on Conditions", *Journal of Aircraft*, vol. 42, no. 1, pp. 245-252.
[9] Van Der Vooren, and Destarac D., (2004), "Drag/thrust analysis of jet-propelled transonic transport aircraft - Definition of physical drag components", *Aerospace Science and Technology*, vol. 8, no. 6, pp. 545-556.
[10] Oswatitsch, K., “Gas Dynamics”, *Academic Press*, New York, 1956, pp.177-210.
[11] Ministry-Industry Drag Analysis Panel Study Group, (1979) “Guide to In-Flight Thrust Measurement of Turbojects and Fan Engines”, AGARD-AG-273, Jan.1979.
[12] “AIAA Drag Prediction Workshop” http://aaac.larc.nasa.gov/tsab/cfdlarc/aiaa-dpw/Workshop2/
[13] “AIAA Drag Prediction Workshop” http://aaac.larc.nasa.gov/tsab/cfdlarc/aiaa-dpw
[14] Brodersen, O. and Stuermer, A. (2001), "Drag prediction of engine-airframe interference effects using unstructured Navier-Stokes calculations", *AIAA Applied Aerodynamics Conference, 19th, Anaheim, CA; UNITED STATES; 11-14 June 2001, AIAA-2001-2414*
[15] Menter, F.R., (1994) “ Two-equation Eddy-Viscosity Turbulance Models for Engineering Applications”. *AIAA Journal* Vol.32, *No.8, August 1994*, pp 1598-1605.